LAWRENCE
LIVERMORE
NATIONAL
LABORATORY

LLNL-JRNL-815884

Scaling of laser-driven electron and proton acceleration as a function of laser pulse duration, energy and intensity in the multi-picosecond regime

R. A. Simpson, G. G. Scott, D. Mariscal, D. Rusby, P. M. King, E. Grace, A. Aghedo, I. Pagano, M. Sinclair, C. Armstrong, M. J. E. Manuel, A. Haid, K. Flippo, L. Winslow, M. Gatu-Johnson, J. A. Frenje, D. Neely, S. Kerr, G. J. Williams, S. Andrews, R. Cauble, K. Charron, R. Costa, B. Fischer, S. Maricle, B. Stuart, F. Albert, N. Lemos, A. Mackinnon, A. MacPhee, A. Pak, T. Ma

October 21, 2020

Physics of Plasmas

Disclaimer

LLNL-JRNL-815884

Scaling of laser-driven electron and proton acceleration as a function of laser pulse duration, energy and intensity in the multi-picosecond regime

R.A. Simpson,[1,2] G.G.Scott,[2] D. Mariscal,[2] D. Rusby,[2] P.M. King,[3,2] E. Grace,[4,2] A. Aghedo,[5] I. Pagano,[3] M. Sinclair,[6] C. Armstrong,[7] M. J.-E. Manuel,[8] A. Haid,[8] K. Flippo,[9] L. Winslow,[1] M. Gatu-Johnson,[1] J.A. Frenje,[1] D. Neely,[7] S. Kerr,[2] G.J. Williams,[2] S.Andrews,[2] R. Cauble,[2] K. Charron,[2] R. Costa,[2] B. Fischer,[2] S. Maricle,[2] B. Stuart,[2] F. Albert,[2] N. Lemos,[2] A. Mackinnon,[2] A. MacPhee,[2] A. Pak,[2] and T. Ma[2]

[1)] *Massachusetts Institute of Technology, Cambridge MA 02139*
[2)] *Lawrence Livermore National Laboratory, Livermore, CA 94550*
[3)] *University of Texas at Austin, Austin, TX 78712*
[4)] *School of Physics, Georgia Institute of Technology, Atlanta, GA 30332*
[5)] *Florida A & M University, Tallahassee, FL 32307*
[6)] *Physics Department, University of California at Los Angeles, Los Angeles, CA*
[7)] *Central Laser Facility, Rutherford Appleton Laboratory, Didcot OX11 0QX, United Kingdom*
[8)] *General Atomics, La Jolla, California 92093, USA*
[9)] *Los Alamos National Laboratory, Los Alamos, New Mexico 87545, USA*

(Dated: 22 October 2020)

A scaling study was conducted of short-pulse laser-driven proton and electron acceleration as a function of pulse duration, laser energy, and laser intensity in the multi-picosecond (ps) regime (∼0.8 ps – 20 ps). Maximum proton energies significantly greater than established scaling laws were observed, consistent with observations at other multi-ps laser facilities. In addition, maximum proton energies and electron temperatures in this regime were found to be strongly dependent on laser pulse duration and pre-plasma conditions. A modified proton scaling model is presented that is able to better represent the accelerated proton characteristics in this multi-ps regime.

I. INTRODUCTION

Over the last two decades, research in laser-driven proton acceleration has emerged as an exciting path for creating compact beam-like sources of MeV protons. In high-energy-density science (HEDS), applications for these sources may include studies in isochoric heating for creating matter at extreme conditions[1], proton radiography of dense targets[2] and proton-induced inertial confinement fusion[3]. An enduring area of research involves studying how laser-driven particle sources can be tailored for this diverse set of applications through a robust understanding of how characteristics of the accelerated protons, such as dose, maximum proton energy and spectral shape scales with key laser parameters, such as pulse duration (τ_{Laser}), focal spot (r_0)[4], laser intensity (I) and laser energy (E_{Laser}).

There are many laser-driven ion acceleration mechanisms that can generate high-energy protons,[5–8] but much of the research on this topic has centered on the target-normal-sheath acceleration (TNSA) process.[9] In TNSA, accelerated protons are produced through high intensity lasers (>10^{18} W/cm^2) impinging on a thin metallic or plastic foil, which is typically ∼5-50 microns thick. During this interaction, the laser ablates material from the front surface of the foil creating a region of underdense plasma blow-off through which electrons are accelerated to significant energies primarily through the ponderomotive force. Electrons with enough energy to escape from the rear of the foil can then establish a strong electric field. Surface contaminants (e.g. water or oils) that are present on the rear of the foil are then accelerated via this sheath field, thereby creating a beam-like source of accelerated ions, with protons preferentially accelerated due to their high charge-to-mass ratio. For laser pulse durations below a picosecond, linearly polarized laser light and steep density gradients, the temperature (T_{hot}) of the hot electrons that drive the sheath field is well-described by the ponderomotive scaling detailed by Wilks[9] and is given by:

$$T_{pond} = m_e c^2 \left(\sqrt{1 + \frac{I[W/cm^2]\lambda^2[\mu m]}{1.37 \times 10^{18}}} - 1 \right). \quad (1)$$

Many scalings exist for the maximum proton energy (E_{max}) obtained in experiments[10–14] and these proton scalings share common characteristics, typically taking the form of $E_{max} \sim \alpha T_{hot}$, where α is a constant. One of the most commonly used scalings was presented by Fuchs *et al.*[11], which is based on a plasma expansion model[13] and incorporates multiple experimental parameters including the laser pulse and target characteristics. This scaling has been shown to capture the relationship between laser intensity and maximum accelerated proton energy for numerous TNSA experiments for pulse durations in the sub-picosecond regime[11,15].

However, recent results using the Advanced Radiographic Capability (ARC) laser at Lawrence Livermore National Laboratory (LLNL)[15] in addition to previous experimental and simulation results at the OMEGA-EP laser at the Laboratory for Laser Energetics[16,17], LFEX-GEKKO laser at the Institute of Laser Engineering[18] and Laser MégaJoule-PETAL[19,20] at the Commissariat à l'Énergie Atomique have demonstrated higher maximum energy protons than would be predicted by the Fuchs model and electron temperatures exceeding the ponderomotive temperature.

These lasers occupy an atypical parameter space when compared to most petawatt-class lasers in that they have relatively long pulse durations (multi-picoseconds), large focal spots (∼10's microns) and are capable of delivering immense

amounts of energy (∼multi-kJ). Many different models[18,21–26] have recently emerged that aim to explain both the enhanced electron and proton characteristics in the multi-picosecond, large focal spot, multi-kJ regime. All of the models largely rely on the fact that large focal spots and longer pulse durations can create long scale-length underdense plasmas with which the laser can interact and accelerate electrons to energies that exceed the ponderomotive scaling. The exact acceleration mechanism is where many of these models diverge. Direct laser acceleration (DLA) is one scheme that has been proposed as the source of these super-ponderomotive electrons.[22,25] In this mechanism, high intensity lasers establish a plasma channel with slowly varying electric fields. Electrons can then oscillate in these fields and gain energy directly from the laser when they are in phase with the laser field[27]. Effective acceleration of the electrons via DLA depends on the scale length of the ion channel and the intensity of the laser. Large focal-spot multi-picosecond lasers create conditions analogous to this mechanism in that the large focal spot can produce long scale-length plasma expansion. This along with the long pulse duration provide conditions where electrons can experience multiple events where they are in phase with, and directly accelerated by, the laser field.[15,22,28]

While many promising models exist, there is an absence of a large data set of TNSA experiments in these conditions. Generating a larger collection of empirical scaling studies will help in the effort to constrain corresponding models. Towards this goal, this paper builds upon the existing scaling studies in laser-driven proton and electron acceleration for laser pulse durations in the sub-picosecond regime[11] by presenting experiments measuring not only characteristics of TNSA protons, but also the hot electron temperature as a function of laser pulse duration for four pulse durations ranging from ∼0.8-20 ps. A summary of all shots taken as part of this study is shown in Table I. Results from these experiments demonstrate that in this regime, the measured temperature of escaping hot electrons far exceed the ponderomotive scaling. In fact, the electron temperatures are enhanced by ∼5-40 times the ponderomotive temperature and underlying these results is a clear dependence on pulse duration and pre-plasma conditions. Consequently, the measured proton energy from these series of experiments is higher than what would be predicted using the Fuchs scaling thus supporting previous proton acceleration measurements in the multi-picosecond regime.

II. EXPERIMENTAL SETUP

This study was conducted with the Titan Laser at the Jupiter Laser Facility (JLF) at Lawrence Livermore National Laboratory.[29] Titan is a neodymium-glass laser system (central wavelength, λ_u= 1.054 μm) that is capable of delivering pulses with durations of 0.7-20 picoseconds with up to 250 J of energy, depending on the pulse length. Uncertainty in the delivered energy is attributed to the systematic error of the calorimetry measurement, which is estimated to be 5%.[30] In order to produce the quasi-relativistic laser intensities (∼10^{18} W/cm^2) that is typical for systems in the large-focal spot, multi-picosecond regime, an f/10 OAP was used to create a larger laser focal spot and depth of field. Titan operated with an f/10 OAP had a r_{50} of 19 ±2 microns. To characterize the statistical error on the focal spot size, multiple images were taken over the duration of the experiment. This error was combined with an assumed systematic error of 10% due to calibration of the focal spot camera.

τ_{Laser} (ps)	E_{Laser} (J)	I_{18} (10^{18} W/cm^2)
0.8 ± 0.2	29 ± 2	3.2± 1.1
0.8 ± 0.2	83 ± 4	9.1± 3.0
0.8 ± 0.2	130 ± 6	14.3± 4.7
2.9 ± 0.6	50 ± 2	1.5± 0.5
2.9 ± 0.6	151 ± 8	4.6± 1.4
11.2 ± 2.4	50 ± 2	0.4± 0.1
11.2 ± 2.4	113 ± 6	0.9± 0.3
11.2 ± 2.4	140 ± 7	1.1± 0.3
11.2 ± 2.4	207 ± 10	1.6± 0.5
20.9 ± 4.2	43 ± 2	0.2± 0.1
20.9 ± 4.2	152 ± 8	0.6± 0.2
20.9 ± 4.2	204 ± 10	0.9± 0.3

TABLE I: Summary of laser energies, intensities and pulse lengths for all shots taken in this scaling study

Shots were performed with multiple pulse lengths and energies to maintain a consistent intensity. For pulse durations below 3 ps, pulse lengths were measured using autocorrelation[31] while a fast optical streak camera was used for longer pulse lengths. Multiple measurements with both diagnostics were taken to define a statistical error on the pulse durations and an additional systematic error of 20% was assumed for both pulse length diagnostics.[32] A significant pre-pulse preceding the main laser pulse, due primarily to reflections in the laser system, is also present for the Titan laser. To characterize the energy and intensity of this pre-pulse, a portion of the main beam is diverted from the main compressor and measured directly by a water cell combined with a photo diode a read out on an oscilloscope. An example oscilloscope trace showing the pre-pulse is plotted in Figure 1.

At each pulse length the laser energy was chosen to scan an intensity range of (10^{17}– 10^{19} W/cm^2), with laser energies spanning ∼30-210 J, on target. Targets were 15 ± 2.25 μm-thick circular aluminum foils that were 3mm in diameter and mounted on silicon washers for support.

Figure 2 illustrates the experimental setup used throughout these series of measurements. To measure the electron spectra and temperature, an Electron-Positron Proton Spectrometer (EPPS)[33] was fielded at 12° relative to target normal. The primary proton diagnostic was a radiochromic film (RCF) stack[34], fielded along the target normal direction. The EPPS diagnostic is a magnetic spectrometer, which uses a permanent magnet to magnetically disperse charged particles based on their gyro-radius. In contrast, an RCF stack, which is comprised of multiple layers of film and aluminum or plastic filters, provides a discrete proton spectrum, the energy-dependent spatial structure of the proton beam, and absolute dose information. Ionizing radiation, in this case predomi-

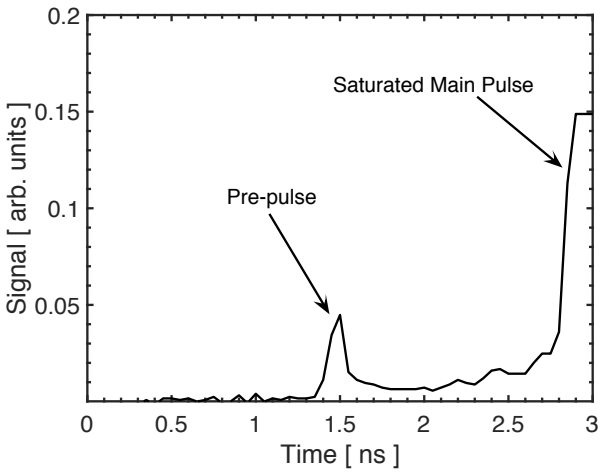

FIG. 1: Example raw data from the watercell diagnostic from one shot ($\tau_{Laser} = 2.9\ ps$, $E_{Laser} = 151J$, $I = 4.6 \times 10^{18}$ W/cm^2) on the Titan laser from this campaign. These watercell measurements were performed on-shot, thus the main laser pulse is saturated on the trace since it has such a high energy and the detector does not have the dynamic range to capture both the full main pulse signal and lower energy pre-pulse. To calibrate this detector, several low energy shots at millijoule energies were taken to relate the signal from the diode to an energy.

nantly protons, causes polymerization of an active dye within the radiochromic film causing the dye to change color in proportion to the deposited dose. In addition, protons lose energy while traversing the stack of films and filters. Given the stopping power of protons in the RCF and filtering material a dose response can be calculated. Therefore, the last layer with a detectable dose can be used to define the maximum proton energy. All reported maximum proton energies from this experiment are from the RCF diagnostic. To obtain absolute dose information, each layer in the RCF stack was scanned using an EPSON EXPRESSION 10000 scanner at a resolution of 300 ppi (pixels per inch). The film pack design used in this work was composed of eight layers of Gafchromic HD-V2 with additional aluminum and plastic filtering, followed by four layers of Gafchromic EBT. EBT is more sensitive than HD-V2, which ensures that the highest energy protons, which also have lower statistics, are recorded and an accurate proton maximum energy can be recorded. In the RCF spectra shown throughout this paper only dose values from the HD-V2 layers are shown since a calibration with this specific scanner for EBT does not currently exist. A 10% systematic error on dose values from the HD-V2 layers was assumed from calibration of the scanner.[35] The first layer of RCF is assumed to be largely contaminated with heavier ions and is also not shown in proton spectra derived fromt the RCF diagnostic. Contributions from x-rays and electrons were also visibly distinct from the main proton beam and subtracted from the primary proton signal on each film.

III. EXPERIMENTAL RESULTS

Example RCF and EPPS spectra measured from three shots from this experiment are plotted in Figure 3: including a short pulse duration high-energy shot (τ_{Laser} = 2.9 ps, E_{laser} = 151 J), a short pulse duration low-energy shot (τ_{Laser} = 2.9 ps, E_{laser} = 50 J) and long pulse-duration, high energy shot (τ_{Laser} = 11.2 ps, E_{laser} = 140 J). Panel (a) shows the RCF-measured proton spectra for these three different shots with varying laser parameters. An exponential curve was fit to each of the spectra to infer a proton slope temperature, thus providing a metric to describe the shape of the measured spectra. Figure 3(b) shows the electron spectra measured by the EPPS diagnostic from the same three shots as panel (a) of Figure 3. Assuming a Maxwellian distribution, fitting the electron spectra with an exponential curve $\frac{dN}{dE} \propto \exp(-E/k_BT)$ can analogously provide a measure of the temperature (T_e) of the population electrons driving the TNSA sheath field. The measured electron distributions presented throughout this paper represents the escaping electron population, which is distinct from the internal electron distribution of electrons trapped within the target. Although, previous work[36–38] has demonstrated these two distributions to be linked.

The intensities for the short pulse duration, low-energy shot (τ_{Laser} = 2.9 ps, E_{laser} = 50 J) and long pulse duration, high-energy shot (τ_{Laser} = 11.2 ps, E_{laser} = 140 J) have similar intensities (I = 1.5 $\times 10^{18}$ W/cm^2 and I = 1.1 $\times 10^{18}$ W/cm^2) and comparing the corresponding proton spectra for these shots shown in Figure 3(a), shows that increasing the pulse length for shots with similar intensities has the effect of increasing the proton slope temperature and overall proton flux. In contrast, considering the long pulse duration, high-energy shot (τ_{Laser} = 11.2 ps, E_{laser} = 140 J) and short pulse duration, high-energy shot (τ_{Laser} = 2.9 ps, E_{laser} = 151 J) which both have similar laser energies, shows that both the proton slope temperature and total proton dose are similar for shots at similar laser energies even though they have different pulse durations. Following similar trends of the inferred proton slope temperatures, the electron temperature increases with longer pulse durations for similar intensity shots, which was a result corroborated by experiments in Mariscal *et al.*[15] and Yogo *et al.*.[18]. Building on these results, comparing the short pulse duration, high energy shot and long pulse duration, high energy shot, shows that shots with similar laser energies have electron slope temperatures within error bars of each other, independent of pulse duration. These example spectra highlight the importance in presenting data in terms of both intensity, laser energy and pulse duration as it serves to decouple which laser parameter has a dominant effect on the resulting particle characteristics. For this reason, all measured data in this paper is presented as a function of both laser energy and laser intensity.

For all pulse lengths scanned, electron temperature measurements inferred from the EPPS spectra are shown in Figure 4(a) as a function of laser energy and in 4(b) as a function of laser intensity. Vertical error bars are due to the uncertainty in the fitting of the electron spectrum. Error bars for the intensity were derived by propagating the uncertainty from

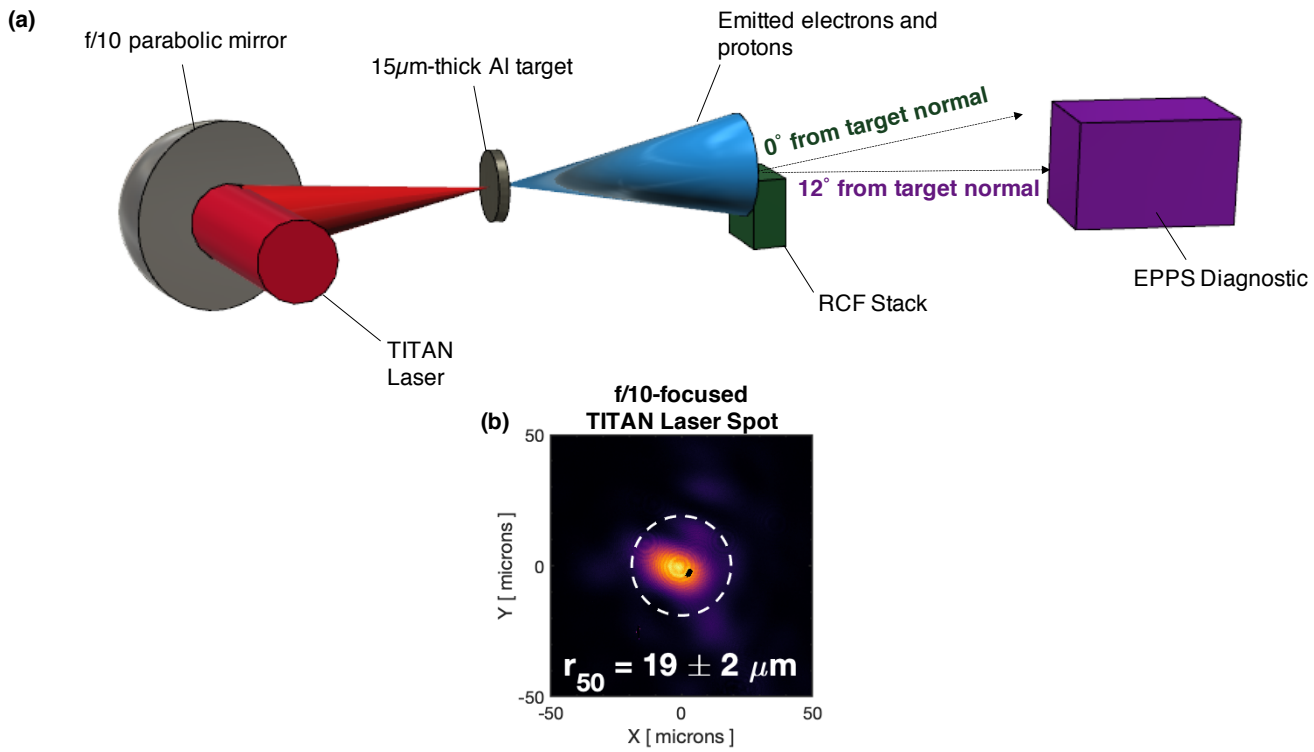

FIG. 2: The full experimental setup used on this campaign is shown in (a). The Titan laser was focused using an f/10 parabolic mirror onto a 15-micron thick aluminum target. The main diagnostics were a radiochromic film stack (RCF) and the electron-positron-proton spectrometer (EPPS). The RCF stack provided measurements of the TNSA proton energies and was placed at 0 degrees relative to the normal of the target, while the EPPS was used to measure electron spectra and was placed 12 degrees from target normal. The aluminum target was irradiated at an angle of 31° relative to the laser axis. The RCF stack was placed 3.5 cm from the target rear surface and the EPPS diagnostic was 70 cm from the target rear surface. In (b) the Titan beam spot (focused with the f/10 parabola) is shown as measured on a low energy, un-amplified pulse. The dashed line shows the radius at which 50% of the energy is contained in the spot.

the focal spot, pulse length and delivered energy measurements. Also, on this plot is the ponderomotive scaling for the hot electron temperature developed by Wilks[9] as well as the Beg temperature scaling described in[39], where $T_{Beg}[MeV] = 0.215(\frac{I[W/cm^2]}{10^{18}}\lambda[\mu m]^2)^{1/3}$ and the Pukhov temperature scaling described in[27], where $T_{Pukhov}[MeV] = 1.5(\frac{I[W/cm^2]}{10^{18}})^{1/2}$. Within each pulse length scan, the measured electron temperatures are consistently a multiplicative factor above their corresponding ponderomotive temperature. For example, within the scan at τ_{Laser}, three shots were completed spanning intensities of 0.2- 0.9 $\times 10^{18}$ W/cm^2 (as shown in Table I). Using the ponderomotive scaling shown in Equation 1, the ponderomotive temperature for these intensities would span $\sim$ 0.040 - 0.16 MeV. However, as shown in Figure 4(b), the measured electron temperature is $\sim$5-40$\times$ higher. To quantitavely describe this enhancement in temperature, the ponderomotive temperature for these three shots were related to the measured electron temperature for these three shots through a linear fit and the slope of this line was taken as the "multiplicative factor " previously described. This process was repeated for each pulse length scan and the multiplicative factor as a function of pulse length is shown in Figure 4(c).

To quantify the pre-plasma conditions on each shot, measurements from the water cell described previously were utilized. This data consistently shows the presence of a pre-pulse at a time of 1.38 ± 0.05ns prior to saturation of the detector on the arrival of the main pulse. Furthermore the duration of the prepulse was measured to be less than 50 ps on all shots, limited by the temporal resolution of the detector. This prepulse is distinct from the amplified spontaneous emission that is also often referred to as the ASE-prepulse and is typically present for nanoseconds prior to the main pulse arrival.

Prepulses have been attributed to many sources, from back reflections in lenses, amplifiers, mirrors and other reflective optic[40,41]. In these instances the prepulse should retain the pulse duration of the main pulse itself and consistently appear at the same time delay before the main pulse. Given the stability of the timing of the pre-pulse, its sub-50 ps duration and its correlation with main pulse energy, it is assumed that the pre-pulse duration has similar duration to the driver laser pulse.

Figure 5(a) shows that for laser energies greater than 80J, and for all pulse durations, the energy in the pre-pulse can be

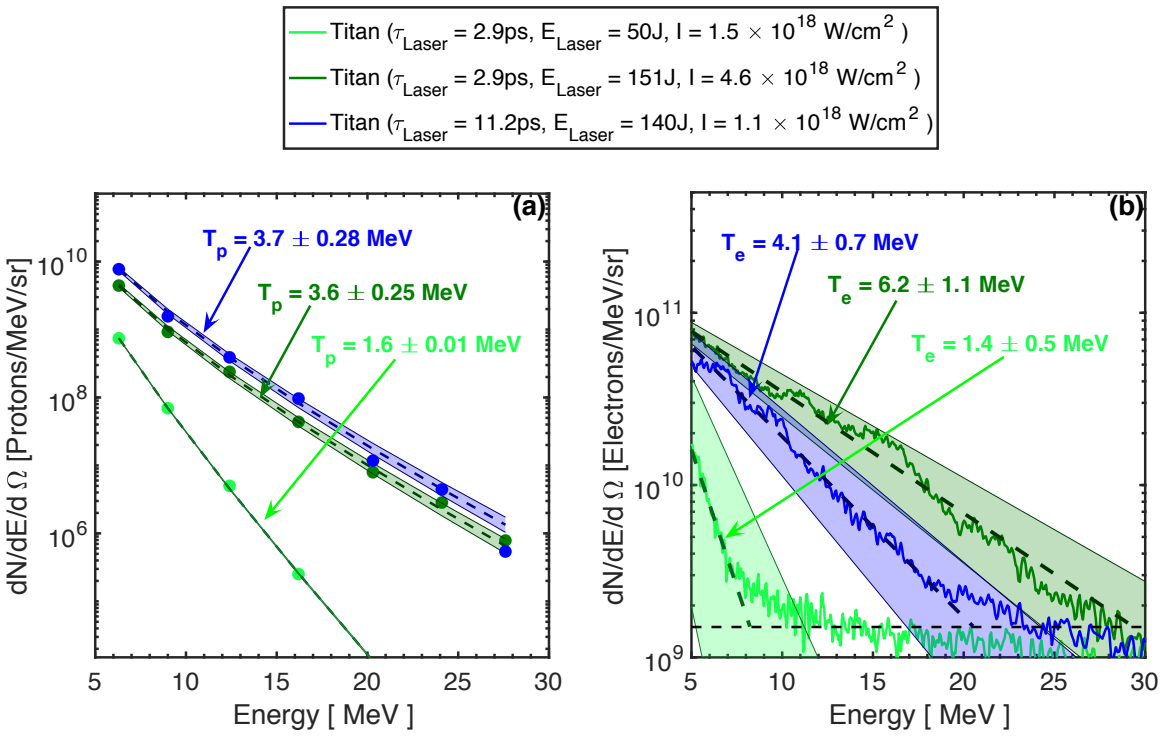

FIG. 3: (a) shows example proton spectra from the RCF stack diagnostic for three shots: a short pulse duration, high-energy shot (shown in dark green, τ_{Laser} = 2.9 ps, E_{laser} = 151 J), a short pulse duration, low-energy shot (shown in light green, τ_{Laser} = 2.9 ps, E_{laser} = 50 J) and long-pulse-duration, high energy shot (shown in dark blue, τ_{Laser} = 11.2 ps, E_{laser} = 140 J). The shaded area for all curves in (a) represents the error in the slope temperature fit. Similarly, (b) shows the electron spectra as measured by the EPPS diagnostic for the same three shots. The shaded region represents the error in the slope temperature fit for the electron measurements.[33]. For both the electron spectra and RCF spectra the slope temperature derived from fitting the spectra with an exponential curve, shows that energy and not intensity has a dominant effect on the temperature regardless of pulse duration.

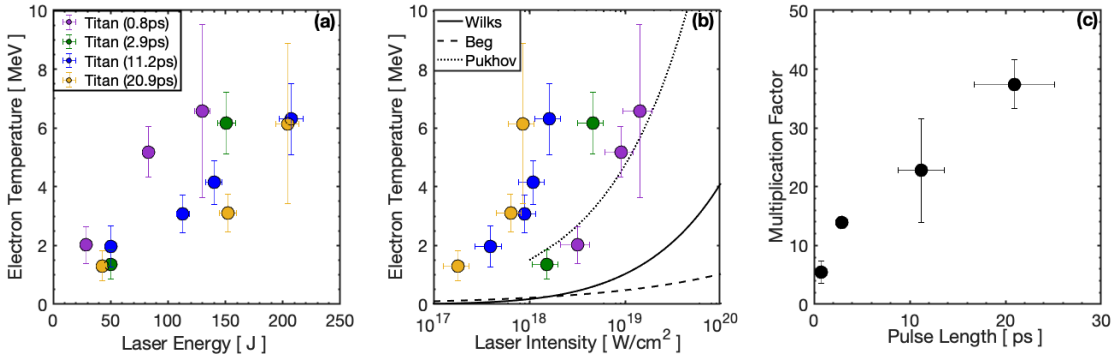

FIG. 4: In panel (a), the solid points show the electron temperature as inferred from the EPPS spectra plotted for each pulse duration investigated as a function of laser energy for varying laser intensity. In panel (b), the same measured electron temperature is shown as a function of laser intensity for varying laser energy. Overlaid on this plot are the Pukhov, Beg and Ponderomotive temperature scalings for reference. The Pukhov scaling is only plotted for intensities about 10^{18} W/cm^2 since this is the regime where this scaling was initially considered. The noise floor of the EPPS diagnostic was 10^9 electrons/MeV/sr. Panel (c) shows the enhancement in the ponderomotive temperature as a function of pulse duration.

easily related to the energy in the main pulse by a fit function shown with the dashed curve in 5(a) . For laser energies lower than this threshold, the pre-pulse is below the signal to noise of the detector. Therefore, to estimate the pre-pulse energy in these shots, the fitting function was used to extrapolate to the lower energies. This was used to estimate the pre-pulse

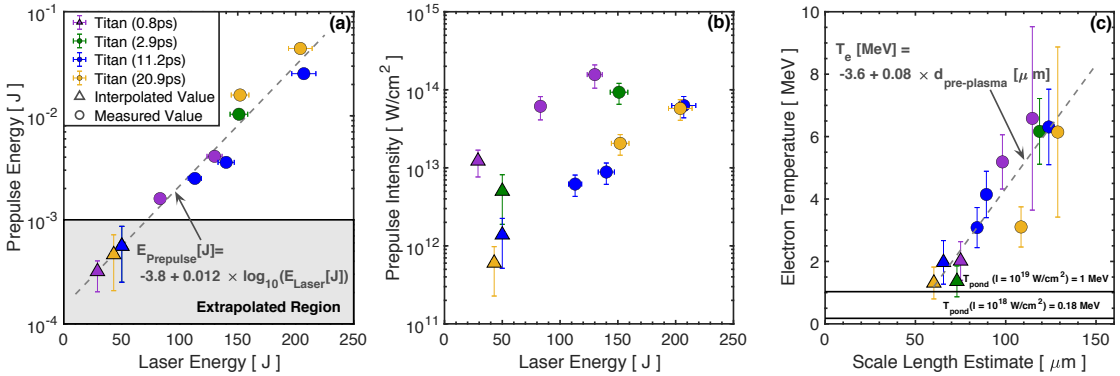

FIG. 5: Panel (a) shows the pre-pulse energy for all shots in this campaign. A subset of shots with main pulse laser energies below ∼50 J had pre-pulse signals below the noise floor and thus these shots have extrapolated values for the pre-pulse energy, which are shown in triangular points instead of circular points. The relationship between pre-pulse energy for each shot and the main laser energy is also shown in the dashed black curve, showing that the pre-pulse energy depends strongly with the main laser energy for each shot. Panel (b) shows the pre-pulse intensity as a function of main pulse laser energy and (c) shows the electron temperature as function of the inferred plasma scale length. Overlaid on this plot in solid black lines are the value of the ponderomotive temperature given by Equation 1 for intensities of 10^{18} and 10^{19} W/cm^2. As the pre-plasma scale length decreases, we would expect the temperature to approach the ponderomotive scaling.

intensity for all shots as shown in Figure 5(b).

This pre-pulse drives plasma expansion in the 1.38 ns prior to the main pulse arrival, and such a plasma expansion has been characterized for plasma mirror interactions[42]. In that work, an analytic plasma expansion model was found to agree well with PIC modelling and experimental data for laser energies in the range of 10-500 mJ, intensities in the range of 10^{13-15} W/cm^2, and pulse durations of 1-40 ps. Since each of these ranges overlap well with the pre-pulse measurements here, we use the scalings reported there to predict the pre-plasma scale length that would be created by the pre-pulse here.

In that work, the electron temperature ($T_{e(RT)}$) driving this scale length evolution was found to be well described by Gibbon's[43] expression for Rozmus and Tikhonchuk's scaling[44], given in equation 2:

$$T_{e(RT)}[eV] = \quad (2)$$
$$119\left(\frac{n_e}{10^{23}cm^{-3}}\right)^{\frac{1}{12}} Z^{\frac{1}{12}} \left(\frac{I}{10^{15}Wcm^{-2}}\right)^{\frac{1}{3}} \left(\frac{\tau_{Laser}}{100fs}\right)^{\frac{1}{6}} (2)$$

With the plasma scale length evolving as $d_{pre-plasma} = c_s t$, where t is the duration of expansion, c_s is the sound speed. Noting that the sound speed is related to the electron temperature by $c_s = \sqrt{\frac{Zk_B T_{e(RT)}^{1/2}}{m_i}}$, an estimate of the scale length can be obtained by substituting the expression for $T_{e(RT)}$ in equation 2 at the time of the main pulse arrival relative to the pre-pulse (Δt).

Noting that in the plasma mirror work, a pre-pulse with an intensity of 10^{14} W/cm^2 and duration of 1 ps initiated a plasma expansion with a scale length of ~ 1 μm after 10 ps, the expression with the substitution can be greatly simplified to equation 2.

$$d_{pre-plasma}[\mu m] = \left(\frac{1\ \mu\text{m}}{10\ \text{ps}}\right)\Delta t(\text{ps})\left(\frac{I_{pre-pulse}}{10^{14}\ \text{Wcm}^{-2}}\right)^{\frac{1}{6}}\left(\frac{\tau_{Laser}}{100\ \text{fs}}\right)^{\frac{1}{12}} \quad (2)$$

where $I_{pre-pulse}$ is the pre-pulse intensity shown in Figure 5(b), and is simply of the form, $d_{pre-plasma} = c_s \Delta t$ multiplied by a correction factor for scaling the intensity and pulse duration of the laser.

The electron temperature, inferred from the EPPS spectra, is plotted as a function of this scale length estimate in 5(c), and shows that the electron temperature linearly increases with the plasma scale length.

Figure 6(a) shows the maximum proton energy inferred from the RCF diagnostic as a function of laser energy and Figure 6(b) details the maximum proton energy as a function of laser intensity. Uncertainty in the maximum proton energy is due to the discrete nature of the RCF diagnostic in that the true maximum energy could lie between the layer with a last visible dose or the one immediately following it. This is shown with asymmetrical error bars in Figure 6(a).

A comparison of the proton temperature and electron temperature is plotted in Figure 6(c) and illustrates their linear relationship. This is unsurprising as the strength of the sheath field is set by the energy of the electrons escaping from the rear surface of the target. The stronger the sheath, the more energetic the protons are that are accelerated. Vertical error bars in the proton temperature are due to the error in the fit. Regardless of pulse length, the electron temperature is roughly a factor of two larger than the proton temperature, which corroborates previous results by Bolton *et al.*[45].

Figure 7 details measurements of the conversion energy and conversion efficiency for all shots. Here, the conversion energy is defined as the total energy into protons > 1 MeV and

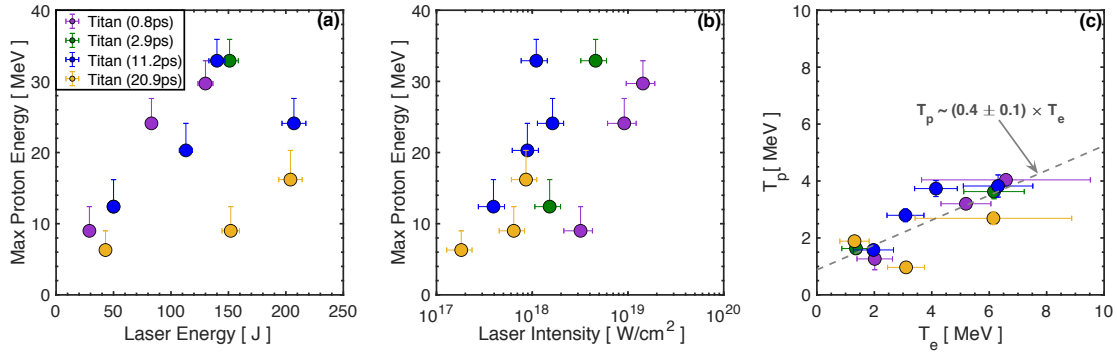

FIG. 6: Panel(a) shows the maximum proton energy measured by the RCF diagnostic as a function of laser energy, whereas panel (b) shows the same information but plotted against laser intensity. Panel (c) shows proton temperature and electron temperature measurements plotted against each other showing that the proton temperature inferred from the RCF diagnostic has a linear relationship with electron temperature inferred from the EPPS for all pulse lengths.

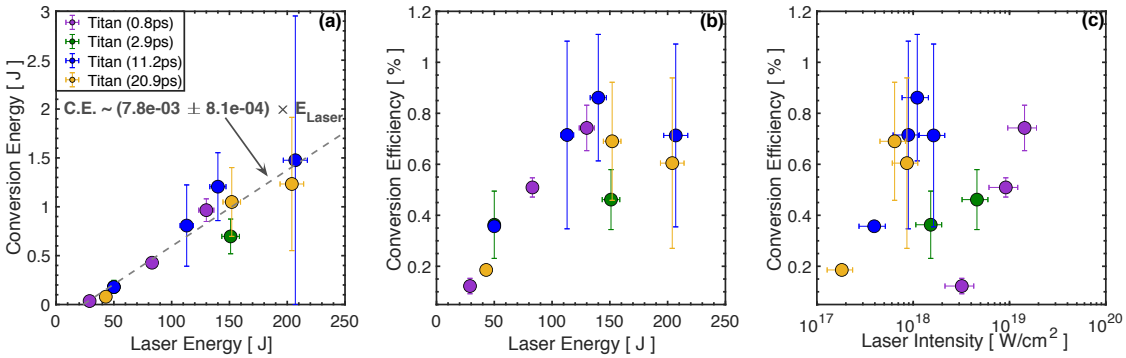

FIG. 7: The total energy into protons $>$ 1 MeV is plotted as a function of laser energy in (a). Conversion efficiency (for protons with energies > 1 MeV) as a function of laser energy is shown in (b) and conversion efficiency (for protons with energies > 1 MeV) is shown as a function of laser intensity in (c).

is plotted as a function of delivered laser energy in Figure 7(a). As expected, this is linear with the laser energy. Figure 7(b) shows the oft-quoted conversion efficiency for protons with energies above 1 MeV as measured by the RCF diagnostic as a function of energy and Figure 7(c) plots the conversion efficiency as a function of laser intensity. Conversion efficiency defined here is the integral of the proton spectrum weighted by the beam divergence (Ω) divided by the laser energy. Proton spectra measured by the RCF diagnostic were fit with an exponential curve of the form $dN/dE \sim \exp(-E/T_{proton})$, such that the conversion efficiency is $\int EdN/dE\Omega dE$ Uncertainty in the calculated conversion efficiency is attributed only to the fit of the spectrum.

The highest conversion efficiency achieved in this work was $\sim$1% at 0.8 ps and an intensity of $\sim 10^{19}$ W/cm^2. However, note that similar conversion efficiencies were accomplished using longer pulse lengths (11.2 and 20.9 ps) at lower laser intensities. This is a result that was also found by Yogo *et al.*[18]. Figure 7 (b) demonstrates that for laser energies above 100 J the conversion efficiency plateaus for the longer pulse durations (i.e. $\geq$ 10 ps) such that energy is no longer being coupled efficiently into the resulting proton beam. Although relatively low conversion efficiencies were achieved in this work, previous work has shown that higher conversion efficiencies can be achieved by using temporally shaped laser pulses[46] and ongoing work is being conducted to study the use of temporally shaped pulses in the multi-ps regime to enhance this coupling[47].

IV. DISCUSSION

The Fuchs model[11] describes the relationship between laser intensity and max proton energy for most TNSA experiments performed with laser pulse lengths in the sub-ps regime. The model follows the common formulation of $E_{max} \propto \alpha T_{hot}$, and relies on the Mora model[13], which is given by:

$$E_{max} = 2T_{hot}\left[\ln[(t_p + (t_p^2+1)^{1/2})]\right], \quad (3)$$

where t_p is the normalized acceleration time. In the Fuchs model, T_{hot} is the Wilks ponderomotive scaling referenced in Equation 1. The normalized acceleration time is given by

$t_p = \omega_{pi}\tau_{acc}/(2\exp(1))$, where τ_{acc} is the acceleration time and ω_{pi} is the ion plasma frequency. In the Fuchs model, τ_{acc} is assumed to be $1.3\tau_{Laser}$. Extending the Fuchs model to the four pulse lengths investigated in this study, which reside in the multi-ps regime, gives the dashed lines shown in Figure 8. All measured maximum proton energies for this study achieve higher proton energies than what would be expected with the Fuchs model.

A modified Fuchs model first described by Rusby[48] relies on the Mora model shown in Equation 3 but adjusts the normalized acceleration time. This modified Fuchs model utilizes a different formalism for τ_{acc}, developed by Brenner *et al.*[49] shown in Equation 4, which has explicit dependence on the laser pulse duration and focal spot size.

$$\tau_{acc} \approx \sqrt{\tau_{Laser}^2 + \tau_{expansion}^2 + \left(\frac{D_{Laser}}{2u_e}\right)^2} \tag{4}$$

The expansion time, $\tau_{expansion}$, uses the Buffechoux *et al.* formulation[50] that is motivated by both experimental results and simulation and is given by $\frac{6}{\omega_{pi}}$. D_{Laser} is the focal spot diameter and for this data set is given by $2 \times r_{50}$. u_e is the average velocity of the electrons. The ion plasma frequency, ω_{pi} is given by: $\sqrt{\frac{e^2 n_e}{\varepsilon_0 m_i}}$, where n_e is the rear surface sheath electron density (assuming quasi-neutrality), and m_i is the proton mass. To calculate the electron density, a model for the sheath size is necessary. Here the sheath size and sheath electron density is given by the same formulation presented by Fuchs[11]. The size of the sheath is dependent on the focal spot size (D_{Laser}), target thickness (d) and angular divergence (θ) of the accelerated electrons, such that the area of the sheath is $S_{sheath} = \pi \times (D_{Laser} + (d \times \tan\theta))$. In the modified Fuchs model, the divergence is based on a collection of empirical results showing the relationship between angular divergence and laser intensity detailed by Green *et al.*[51]. A fit to this compilation of data gives the result, $\theta \sim 6.45\ln(I[W/cm^2]/1\times10^{18}) - 257.24$.[52] The electron density is then given by, as described in[11], as: $n_{e0} = N_e/(c\tau_{Laser}S_{sheath})$, where N_e is the total number of electrons and is equal to $1.2\times10^{-15}E_{laser}/T_{hot}$.

In addition to these modifications, for this specific data set taken at Titan, T_{hot} was modified from the ponderomotive scaling that is used in the Fuchs model. To investigate the impact of different temperature models on this modified model, three different temperature models for T_{hot} were tried: (1) $T_{hot} = T_{Pukhov}$, (2) $T_{hot} = 5\times T_{Beg}$ and (3) $T_{hot} = 5\times T_{pond}$. In Figure 4 (c), the multiplication factor in comparing the ponderomotive electron temperature and measured electron temperature within each pulse length scan is plotted and is shown to span $\sim$ 5-40$\times$ the ponderomotive scaling depending on the pulse length. However, using an enhanced factor of 5 for the models using the Beg temperature scaling and ponderomotive scaling in the modified Fuchs model best captures the maximum proton energy scaling for all pulse lengths in this study. Since the Fuchs model scales linearly with T_{hot}, modifying this parameter has the largest effect in making the modified Fuchs model fit the measured points. The measured electron temperature shown in Figure 4(b) provides some justification for increasing the electron temperature in the model given that all measured temperatures are well above the ponderomotive temperature for all intensities and pulse lengths. In addition, the inferred pre-plasma scale length shown in Figure 5(c) shows a linear relationship between the measured electron temperature and inferred pre-plasma scale length. This is a result that is consistent with electron acceleration from direct laser acceleration (DLA), in which the electron energy gain is proportional to the length of underdense plasma that the electron is accelerated within and this may provide hints that this is a candidate mechanism for the measured increased electron temperatures. To investigate this mechanism directly, future work will include dedicated experiments to measure direct laser acceleration in this multi-ps regime.

The resulting curves using the modified Fuchs model, with the different temperature models, are plotted for the four pulse lengths investigated in solid curves on Figure 8(a)-(c). The model that best captures the measured data is shown in Figure 8(c), which uses $T_{hot} = 5\times T_{pond}$ for the temperature scaling. For this model, the coefficient of determination or R^2 values for each pulse length scan ($\tau_{Laser} = [0.8, 2.9, 11.2, 20.9]$ps) comparing the measured data and Fuchs model are $R^2_{Fuchs} = [0.22, -0.70, -4.4, -1.3]$, whereas the modified Fuchs model, has R^2 values of $R^2_{Modified-Fuchs} = [0.95, 0.99, 0.19, -3.12]$. The modified Fuchs model with $T_{hot} = 5\times T_{pond}$ better captures the relationship between intensity and maximum proton energy for all pulse lengths scanned except at 20 ps. In addition, this modified Fuchs model also better describes the maximum proton energy vs. laser intensity scaling for the 0.8 ps data, which has a pulse duration on the margins of the sub-ps/multi-ps boundary. This may be due to the enhanced pre-plasma created by significant pre-pulse on the Titan laser creating conditions for a hotter electron temperature distribution. Figure 8(a), which shows the modified Fuchs model with $T_{hot} = T_{Pukhov}$ also has good agreement with data. However, the modified model with this temperature scaling is only plotted over the intensities where the T_{Pukhov} was studied, which is greater than 10^{18} W/cm^2.

The modified Fuchs model was also applied to previous TNSA results on other multi-ps facilities, including OMEGA-EP, LFEX-GEKKO and NIF-ARC. Figure 9(a) - (c) plots both the Fuchs model and modified Fuchs model for all of these data sets. For all plots in Figure 9, T_{pond} was enhanced by a factor of five in the same way that was done for the Titan results. Like the Titan data set, most measured points across all three facilities have proton energies that exceed the Fuchs scaling, but unlike the Titan data set, they are not well captured by the modified Fuchs model. Enhancing the hot electron temperature by 5$\times$ the ponderomotive scaling was a simple constant parameter included to the modified Fuchs model to fit the measured data from Titan specifically. However, Figure 5(c) demonstrates that the electron temperature is strongly dependent on pre-plasma conditions, which vary widely across laser facilities based on the laser contrast. While in this work, the derived pre-plasma scale length is shown to be linked with the main pulse laser energy, this relationship may also vary across laser faciliities and thus motivates the need to fully characterize delivered laser pulses. Therefore,

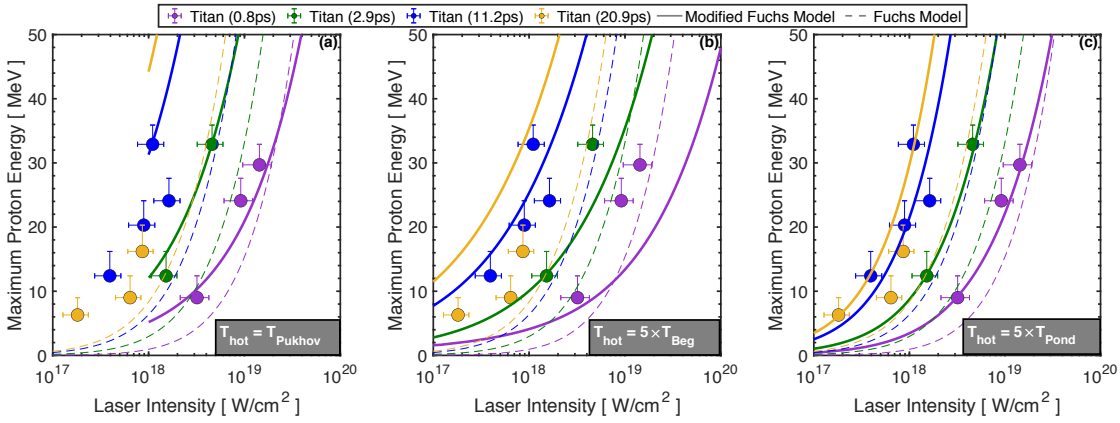

FIG. 8: In each panel, the maximum proton energy measured by the RCF diagnostic as a function of laser intensity. Plotted in dashed curves is the Fuchs model for each pulse length investigated. In solid curves is the modified Fuchs model. In panel (a) the modified models uses the Pukhov temperature scaling for T_{hot}. The modified Fuchs model in Panel (a) is only plotted for intensities where the Pukhov model is valid, which is greater than 10^{18} W/cm^2. Panel(b) uses the Beg scaling for temperature multiplied by a factor of 5 and panel (c) uses the ponderomotive scaling for temperature multiplied by a factor of 5.

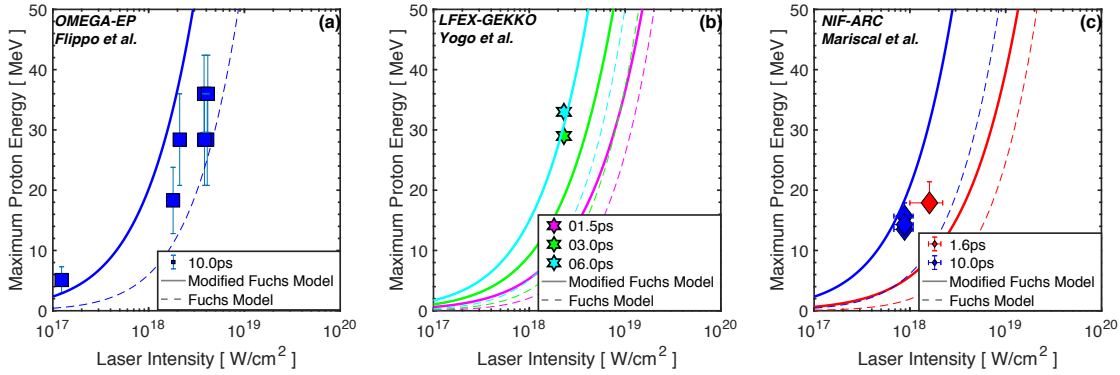

FIG. 9: (a)-(c) shows the modified Fuchs model being applied to previous TNSA proton data sets taken on OMEGA-EP, LFEX-GEKKO and NIF-ARC.

future improvements to this model may include an explicit dependence of the maximum proton energy on pre-plasma scale length.

V. CONCLUSIONS

The results of this scaling study show that in the multi-picosecond regime, maximum TNSA proton energy exceeds that which would be predicted by the Fuchs model, which does capture the dynamics of TNSA proton acceleration for pulse lengths below ~1 ps. These measurements corroborate results demonstrated by other lasers in the large focal spot, multi-picosecond, multi-kJ regime. A modified Fuchs model that incorporates the enhanced electron temperature has been found to better capture the data presented in this study. In addition, measured electron temperatures for this pulse length scan show that this enhanced TNSA may be due to a population of super-ponderomotive electrons that establish the accelerating sheath field. Estimates of the pre-plasma scale length based on measurements of the pre-pulse energy show a strong correlation between the measured electron temperature and the pre-plasma scale length. This long pre-plasma scale length may enable conditions that are advantageous for the production of these super-ponderomotive electrons. Future research will include experimental work in investigating direct laser acceleration as a candidate mechanism for enhanced electron acceleration in the multi-ps regime.

VI. ACKNOWLEDGEMENTS

The authors would like to thank the Jupiter Laser Facility staff for without their expertise the experiment detailed here would not have been possible. The authors would also like to thank Alex Haid at General Atomics for his work in assembling the targets used in this experiment under NNSA contract DE-NA0001808. This work was completed under the auspices of the U.S. Department of Energy by Lawrence Livermore National Laboratory under contract

DE-AC52-07NA27344 with funding support from the Laboratory Directed Research and Development Program under tracking code 17-ERD-039 and 20-ERD-048, the DOE Office of Science Early Career Research Program under SCW1651, and the Department of Energy National Nuclear Security Administration Laboratory Residency Graduate Fellowship program, which is provided under grant number DE-NA0003864.

VII. REFERENCES

[1] R. A. Snavely, B. Zhang, K. Akli, Z. Chen, R. R. Freeman, P. Gu, S. P. Hatchett, D. Hey, J. Hill, M. H. Key, Y. Izawa, J. King, Y. Kitagawa, R. Kodama, A. B. Langdon, B. F. Lasinski, A. Lei, A. J. MacKinnon, P. Patel, R. Stephens, M. Tampo, K. A. Tanaka, R. Town, Y. Toyama, T. Tsutsumi, S. C. Wilks, T. Yabuuchi, and J. Zheng. Laser generated proton beam focusing and high temperature isochoric heating of solid matter. *Physics of Plasmas*, 14(9):092703, 2007.

[2] A. B. Zylstra, C. K. Li, H. G. Rinderknecht, F. H. Séguin, R. D. Petrasso, C. Stoeckl, D. D. Meyerhofer, P. Nilson, T. C. Sangster, S. Le Pape, A. Mackinnon, and P. Patel. Using high-intensity laser-generated energetic protons to radiograph directly driven implosions. *Review of Scientific Instruments*, 83(1):013511, 2012.

[3] M. Roth, T. E. Cowan, M. H. Key, S. P. Hatchett, C. Brown, W. Fountain, J. Johnson, D. M. Pennington, R. A. Snavely, S. C. Wilks, K. Yasuike, H. Ruhl, F. Pegoraro, S. V. Bulanov, E. M. Campbell, M. D. Perry, and H. Powell. Fast ignition by intense laser-accelerated proton beams. *Phys. Rev. Lett.*, 86:436–439, 2001.

[4] C.M. Brenner, J.S. Green, A.P.L. Robinson, D.C. Carroll, B. Dromey, P.S. Foster, S. Kar, Y.T. Li, K. Markey, C. Spindloe, and et al. Dependence of laser accelerated protons on laser energy following the interaction of defocused, intense laser pulses with ultra-thin targets. *Laser and Particle Beams*, 29(3):345–351, 2011.

[5] Bin Qiao, Xiaofei Shen, Hao He, Yu Xie, Hua Zhang, Cangtao Zhou, Shaoping Zhu, and Xian-tu He. Revisit on ion acceleration mechanisms in solid targets driven by intense laser pulses. *Plasma Physics and Controlled Fusion*, 61, 2018.

[6] A. Higginson, R. J. Gray, M. King, R. J. Dance, S. D.R. Williamson, N. M.H. Butler, R. Wilson, R. Capdessus, C. Armstrong, J. S. Green, S. J. Hawkes, P. Martin, W. Q. Wei, S. R. Mirfayzi, X. H. Yuan, S. Kar, M. Borghesi, R. J. Clarke, D. Neely, and P. McKenna. Near-100 MeV protons via a laser-driven transparency-enhanced hybrid acceleration scheme. *Nature Communications*, 9(724), 2018.

[7] S. Kar, K. F. Kakolee, B. Qiao, A. Macchi, M. Cerchez, D. Doria, M. Geissler, P. McKenna, D. Neely, J. Osterholz, R. Prasad, K. Quinn, B. Ramakrishna, G. Sarri, O. Willi, X. Y. Yuan, M. Zepf, and M. Borghesi. Ion acceleration in multispecies targets driven by intense laser radiation pressure. *Phys. Rev. Lett.*, 109:185006, 2012.

[8] A P L Robinson, M Zepf, S Kar, R G Evans, and C Bellei. Radiation pressure acceleration of thin foils with circularly polarized laser pulses. *New Journal of Physics*, 10(1):013021, 2008.

[9] S. C. Wilks, A. B. Langdon, T. E. Cowan, M. Roth, M. Singh, S. Hatchett, M. H. Key, D. Pennington, A. MacKinnon, and R. A. Snavely. Energetic proton generation in ultra-intense laser–solid interactions. *Physics of Plasmas*, 8(2):542–549, 2001.

[10] J. Denavit. Collisionless plasma expansion into a vacuum. *The Physics of Fluids*, 22(7):1384–1392, 1979.

[11] J. Fuchs, P. Antici, E. D'Humières, E. Lefebvre, M. Borghesi, E. Brambrink, C. A. Cecchetti, M. Kaluza, V. Malka, M. Manclossi, S. Meyroneinc, P. Mora, J. Schreiber, T. Toncian, H. Pépin, and P. Audebert. Laser-driven proton scaling laws and new paths towards energy increase. *Nature Physics*, 2:48–54, 2006.

[12] S. J. Gitomer, R. D. Jones, F. Begay, A. W. Ehler, J. F. Kephart, and R. Kristal. Fast ions and hot electrons in the laser–plasma interaction. *The Physics of Fluids*, 29(8):2679–2688, 1986.

[13] P. Mora. Plasma expansion into a vacuum. *Phys. Rev. Lett.*, 90:185002, 2003.

[14] M. Tampo, S. Awano, P. R. Bolton, K. Kondo, K. Mima, Y. Mori, H. Nakamura, M. Nakatsutsumi, R. B. Stephens, K. A. Tanaka, T. Tanimoto, T. Yabuuchi, and R. Kodama. Correlation between laser accelerated mev proton and electron beams using simple fluid model for target normal sheath acceleration. *Physics of Plasmas*, 17(7):073110, 2010.

[15] D. Mariscal, T. Ma, S. C. Wilks, A. J. Kemp, G. J. Williams, P. Michel, H. Chen, P. K. Patel, B. A. Remington, M. Bowers, L. Pelz, M. R. Hermann, W. Hsing, D. Martinez, R. Sigurdsson, M. Prantil, A. Conder, J. Lawson, M. Hamamoto, P. Di Nicola, C. Widmayer, D. Homoelle, R. Lowe-Webb, S. Herriot, W. Williams, D. Alessi, D. Kalantar, R. Zacharias, C. Haefner, N. Thompson, T. Zobrist, D. Lord, N. Hash, A. Pak, N. Lemos, M. Tabak, C. McGuffey, J. Kim, F. N. Beg, M. S. Wei, P. Norreys, A. Morace, N. Iwata, Y. Sentoku, D. Neely, G. G. Scott, and K. Flippo. First demonstration of arc-accelerated proton beams at the national ignition facility. *Physics of Plasmas*, 26(4):043110, 2019.

[16] Kirk Flippo, Teresa Bartal, Farhat Beg, Sugreev Chawla, Jim Cobble, Sandrine Gaillard, Daniel Hey, Andrew Mackinnon, Andrew Macphee, Phillip Nilson, Dustin Offermann, Sebastien Pape, and Mark Schmitt. Omega ep, laser scalings and the 60 mev barrier: First observations of ion acceleration performance in the 10 picosecond kilojoule short-pulse regime. *Journal of Physics: Conference Series*, 244:022033, 2010.

[17] Paul T Campbell, D Canning, A E Hussein, K D W Ratnayaka, A G R Thomas, K Krushelnick, and L Willingale. Proton beam emittance growth in multipicosecond laser-solid interactions. *New Journal of Physics*, 21(10):103021, 2019.

[18] A. Yogo, K. Mima, N. Iwata, S. Tosaki, A. Morace, Y. Arikawa, S. Fujioka, T. Johzaki, Y. Sentoku, H. Nishimura, A. Sagisaka, K. Matsuo, N. Kamitsukasa, S. Kojima, H. Nagatomo, M. Nakai, H. Shiraga, M. Murakami, S. Tokita, J. Kawanaka, N. Miyanaga, K. Yamanoi, T. Norimatsu, H. Sakagami, S. V. Bulanov, K. Kondo, and H. Azechi. Boosting laser-ion acceleration with multi-picosecond pulses. *Scientific Reports*, 7(42451), 2017.

[19] J.E. Ducret, Dimitri Batani, Guillaume Boutoux, Antoine Chance, Bernard Gastineau, J.-C Guillard, F. Harrault, Katarzyna Jakubowska, Isabelle Thfoin, D. Leboeuf, D. Loiseau, A. Lotode, Chhon Pes, Nesrine Rabhi, A. Saïd, A. Semsoum, Laurent Serani, B. Thomas, J.-C Toussaint, and Benjamin Vauzour. Calibration of the low-energy channel thomson parabola of the lmj-petal diagnostic sepage with protons and carbon ions. *Review of Scientific Instruments*, 89:023304, 2018.

[20] Emmanuel d'Humieres. Ion acceleration by high intensity short pulse lasers. In Igor Peshko, editor, *Laser Pulses*, chapter 11. IntechOpen, Rijeka, 2012.

[21] Natsumi Iwata, Kunioki Mima, Yasuhiko Sentoku, Akifumi Yogo, Hideo Nagatomo, Hiroaki Nishimura, and Hiroshi Azechi. Fast ion acceleration in a foil plasma heated by a multi-picosecond high intensity laser. *Physics of Plasmas*, 24(7):073111, 2017.

[22] A. Kemp. Direct Electron Acceleration in Multi-Kilojoule, Multi-Picosecond Laser Pulses. 61st Annual Meeting of the APS Division of Plasma Physics, 2019.

[23]Sadaoki Kojima, Masayasu Hata, Natsumi Iwata, Yasunobu Arikawa, Alessio Morace, Shohei Sakata, Seungho Lee, Kazuki Matsuo, King Fai Farley Law, Hiroki Morita, Yugo Ochiai, Akifumi Yogo, Hideo Nagatomo, Tetsuo Ozaki, Tomoyuki Johzaki, Atsushi Sunahara, Hitoshi Sakagami, Zhe Zhang, Shota Tosaki, Yuki Abe, Junji Kawanaka, Shigeki Tokita, Mitsuo Nakai, Hiroaki Nishimura, Hiroyuki Shiraga, Hiroshi Azechi, Yasuhiko Sentoku, and Shinsuke Fujioka. Electromagnetic field growth triggering super-ponderomotive electron acceleration during multi-picosecond laser-plasma interaction. *Communications Physics*, 2(99), 2019.

[24]G. J. Williams, A. Link, M. Sherlock, D. A. Alessi, M. Bowers, A. Conder, P. Di Nicola, G. Fiksel, F. Fiuza, M. Hamamoto, M. R. Hermann, S. Herriot, D. Homoelle, W. Hsing, E. d'Humières, D. Kalantar, A. Kemp, S. Kerr, J. Kim, K. N. LaFortune, J. Lawson, R. Lowe-Webb, T. Ma, D. A. Mariscal, D. Martinez, M. J.-E. Manuel, M. Nakai, L. Pelz, M. Prantil, B. Remington, R. Sigurdsson, C. Widmayer, W. Williams, L. Willingale, R. Zacharias, K. Youngblood, and Hui Chen. Production of relativistic electrons at subrelativistic laser intensities. *Phys. Rev. E*, 101:031201, 2020.

[25]A. Sorokovikova, A. V. Arefiev, C. McGuffey, B. Qiao, A. P. L. Robinson, M. S. Wei, H. S. McLean, and F. N. Beg. Generation of superponderomotive electrons in multipicosecond interactions of kilojoule laser beams with solid-density plasmas. *Phys. Rev. Lett.*, 116:155001, 2016.

[26]A. G. Krygier, D. W. Schumacher, and R. R. Freeman. On the origin of super-hot electrons from intense laser interactions with solid targets having moderate scale length preformed plasmas. *Physics of Plasmas*, 21(2):023112, 2014.

[27]A. Pukhov, Z.-M. Sheng, and J. Meyer-ter Vehn. Particle acceleration in relativistic laser channels. *Physics of Plasmas*, 6(7):2847–2854, 1999.

[28]Amina Hussein. Optimizing Direct Laser Acceleration. In *APS Division of Plasma Physics Meeting Abstracts*, volume 2019 of *APS Meeting Abstracts*, page NI3.004, 2019.

[29]B. C. Stuart, J. D. Bonlie, J. A. Britten, J. A. Caird, R. R. Cross, C. A. Ebbers, M. J. Eckart, A. C. Erlandson, W. A. Molander, A. Ng, P. K. Patel, and D. F. Price. The Titan laser at LLNL. In *Conference on Lasers and Electro-Optics and 2006 Quantum Electronics and Laser Science Conference, CLEO/QELS 2006*, 2006.

[30]Stephen Maricle. Private Communication.

[31]M. Maier, W. Kaiser, and J. A. Giordmaine. Intense light bursts in the stimulated raman effect. *Phys. Rev. Lett.*, 17:1275–1277, 1966.

[32]Scott Andrews. Private Communication.

[33]Hui Chen, Anthony Link, Roger Maren, Pravesh Patel, Ronnie Shepherd, Scott Wilks, and Peter Beiersdorfer. High performance compact magnetic spectrometers for energetic ion and electron measurement in ultraintense short pulse laser solid interactions. *The Review of scientific instruments*, 79:10E533, 2008.

[34]F. Nürnberg, M. Schollmeier, E. Brambrink, A. Blažević, D. C. Carroll, K. Flippo, D. C. Gautier, M. Geißel, K. Harres, B. M. Hegelich, O. Lundh, K. Markey, P. McKenna, D. Neely, J. Schreiber, and M. Roth. Radiochromic film imaging spectroscopy of laser-accelerated proton beams. *Review of Scientific Instruments*, 80(3):033301, 2009.

[35]Graeme Gordon Scott. Private Communication.

[36]A. Link, R. R. Freeman, D. W. Schumacher, and L. D. Van Woerkom. Effects of target charging and ion emission on the energy spectrum of emitted electrons. *Physics of Plasmas*, 18(5):053107, 2011.

[37]P Antici, B Albertazzi, P Audebert, S Buffechoux, F Hannachi, E dHumières, F Gobet, T Grismayer, A Mancic, M Nakatsutsumi, C Plaisir, L Romagnani, M Tarisien, H Pépin, Y Sentoku, and J Fuchs. Measuring hot electron distributions in intense laser interaction with dense matter. *New Journal of Physics*, 14(6):063023, 2012.

[38]D. R. Rusby, C. D. Armstrong, G. G. Scott, M. King, P. McKenna, and D. Neely. Effect of rear surface fields on hot, refluxing and escaping electron populations via numerical simulations. *High Power Laser Science and Engineering*, 7:e45, 2019.

[39]M. G. Haines, M. S. Wei, F. N. Beg, and R. B. Stephens. Hot-electron temperature and laser-light absorption in fast ignition. *Phys. Rev. Lett.*, 102:045008, 2009.

[40]E Gaul, T Toncian, M Martinez, J Gordon, M Spinks, G Dyer, N Truong, C Wagner, G Tiwari, M E Donovan, T Ditmire, and B M Hegelich. Improved pulse contrast on the texas petawatt laser. *Journal of Physics: Conference Series*, 717:012092, 2016.

[41]Josef Cupal, Thomas Spinka, Emily Sistrunk, Bedrich Rus, and Constantin Haefner. Temporal pre-pulse generation in high-intensity CPA lasers from imperfect domain orientation in anisotropic crystals. In Pavel Bakule and Constantin L. Haefner, editors, *Short-pulse High-energy Lasers and Ultrafast Optical Technologies*, volume 11034, pages 24 – 33. International Society for Optics and Photonics, SPIE, 2019.

[42]G G Scott, V Bagnoud, C Brabetz, R J Clarke, J S Green, R I Heathcote, H W Powell, B Zielbauer, T D Arber, P McKenna, and D Neely. Optimization of plasma mirror reflectivity and optical quality using double laser pulses. *New Journal of Physics*, 17(3):033027, 2015.

[43]P Gibbon and E Förster. Short-pulse laser - plasma interactions, 1996.

[44]W. Rozmus and V. T. Tikhonchuk. Skin effect and interaction of short laser pulses with dense plasmas. *Phys. Rev. A*, 42:7401–7412, 1990.

[45]P.R. Bolton, M. Borghesi, C. Brenner, D.C. Carroll, C. De Martinis, F. Fiorini, A. Flacco, V. Floquet, J. Fuchs, P. Gallegos, D. Giove, J.S. Green, S. Green, B. Jones, D. Kirby, P. McKenna, D. Neely, F. Nuesslin, R. Prasad, S. Reinhardt, M. Roth, U. Schramm, G.G. Scott, S. Ter-Avetisyan, M. Tolley, G. Turchetti, and J.J. Wilkens. Instrumentation for diagnostics and control of laser-accelerated proton (ion) beams. *Physica Medica*, 30(3):255 – 270, 2014.

[46]C. M. Brenner, A. P.L. Robinson, K. Markey, R. H.H. Scott, R. J. Gray, M. Rosinski, O. Deppert, J. Badziak, D. Batani, J. R. Davies, S. M. Hassan, K. L. Lancaster, K. Li, I. O. Musgrave, P. A. Norreys, J. Pasley, M. Roth, H. P. Schlenvoigt, C. Spindloe, M. Tatarakis, T. Winstone, J. Wolowski, D. Wyatt, P. McKenna, and D. Neely. High energy conversion efficiency in laser-proton acceleration by controlling laser-energy deposition onto thin foil targets. *Applied Physics Letters*, 2014.

[47]J. Kim, A. J. Kemp, S. C. Wilks, D. H. Kalantar, S. Kerr, D. Mariscal, F. N. Beg, C. McGuffey, and T. Ma. Computational modeling of proton acceleration with multi-picosecond and high energy, kilojoule, lasers. *Physics of Plasmas*, 2018.

[48]Dean Richard Rusby. *Study of Escaping Electron Dynamics and Applications from High-Power Laser-Plasma Interactions*. PhD thesis, 2017.

[49]C M Brenner, P McKenna, and D Neely. Modelling the effect of laser focal spot size on sheath- accelerated protons in intense laser–foil interactions. *Plasma Physics and Controlled Fusion*, 56(8):084003, 2014.

[50]S. Buffechoux, J. Psikal, M. Nakatsutsumi, L. Romagnani, A. Andreev, K. Zeil, M. Amin, P. Antici, T. Burris-Mog, A. Compant-La-Fontaine, E. d'Humières, S. Fourmaux, S. Gaillard, F. Gobet, F. Hannachi, S. Kraft, A. Mancic, C. Plaisir, G. Sarri, M. Tarisien, T. Toncian, U. Schramm, M. Tampo, P. Audebert, O. Willi, T. E. Cowan, H. Pépin, V. Tikhonchuk, M. Borghesi, and J. Fuchs. Hot electrons transverse refluxing in ultraintense laser-solid interactions. *Phys. Rev. Lett.*, 105:015005, 2010.

[51]J. S. Green, V. M. Ovchinnikov, R. G. Evans, K. U. Akli, H. Azechi, F. N. Beg, C. Bellei, R. R. Freeman, H. Habara, R. Heathcote, M. H. Key, J. A. King, K. L. Lancaster, N. C. Lopes, T. Ma, A. J. MacKinnon, K. Markey, A. McPhee, Z. Najmudin, P. Nilson, R. Onofrei, R. Stephens, K. Takeda, K. A. Tanaka, W. Theobald, T. Tanimoto, J. Waugh, L. Van Woerkom, N. C. Woolsey, M. Zepf, J. R. Davies, and P. A. Norreys. Effect of laser intensity on fast-electron-beam divergence in solid-density plasmas. *Phys. Rev. Lett.*, 100:015003, 2008.

[52]C D Armstrong, C M Brenner, E Zemaityte, G G Scott, D R Rusby, G Liao, H Liu, Y Li, Z Zhang, Y Zhang, B Zhu, P Bradford, N C Woolsey, P Oliveira, C Spindloe, W Wang, P McKenna, and D Neely. Bremsstrahlung emission profile from intense laser-solid interactions as a function of laser focal spot size. *Plasma Physics and Controlled Fusion*, 61(3):034001, 2019.

VIII. DATA AVAILABILITY STATEMENT

The data that support the findings of this study are available from the corresponding author upon request.